THE JOURNAL OF PHYSICAL CHEMISTRY C

Article

Cite This: J. Phys. Chem. C 2018, 122, 11709−11719

pubs.acs.org/JPCC

# High-Resolution Imaging of Polymer Electrolyte Membrane Fuel Cell Cathode Layers by Soft X-ray Spectro-Ptychography

Juan Wu,[†] Xiaohui Zhu,[†] Marcia M. West,[‡] Tolek Tyliszczak,[§] Hung-Wei Shiu,[§,∥] David Shapiro,[§] Viatcheslav Berejnov,[⊥] Darija Susac,[⊥] Juergen Stumper,[⊥] and Adam P. Hitchcock*[,†]

[†]Dept. of Chemistry and Chemical Biology, McMaster University, Hamilton L8S 4M1, Ontario, Canada

[‡]Electron Microscopy, Dept. of Pathology, McMaster University, Hamilton, Ontario L8N 3Z5, Canada

[§]Advanced Light Source, Berkeley Laboratory, Berkeley, California 94720, United States

[∥]National Synchrotron Radiation Research Center, Hsinchu, Taiwan 30076, R.O.C.

[⊥]AFCC, 9000 Glenlyon Parkway, Burnaby, British Columbia V5J 5J8, Canada

Supporting Information

**ABSTRACT:** Polymer electrolyte membrane fuel cells (PEMFCs) are a promising and sustainable alternative to internal combustion engines for automotive applications. Polymeric perfluorosulfonic acid (PFSA) plays a key role in PEMFCs as a proton conductor in the anode and cathode catalyst layers and in the electrolyte membrane. In this study, spectroscopic scanning coherent diffraction imaging (spectro-ptychography) and spectro-ptychographic tomography were used to quantitatively image PFSA ionomers in PEMFC cathodes in both two and three dimensions. We verify that soft X-ray ptychography gives significant spatial resolution improvement on soft matter polymeric materials. A two-dimensional spatial resolution of better than 15 nm was achieved. With better detectors and brighter and more coherent X-ray beams, radiation-sensitive PFSA ionomers will be visualized with acceptable levels of chemical and structural modification. This work is a step toward visualization of ionomers in PEMFC cathodes at high spatial resolution (presently sub-15 nm, but ultimately below 10 nm), which will be transformative with respect to optimization of PEMFCs for automotive use.

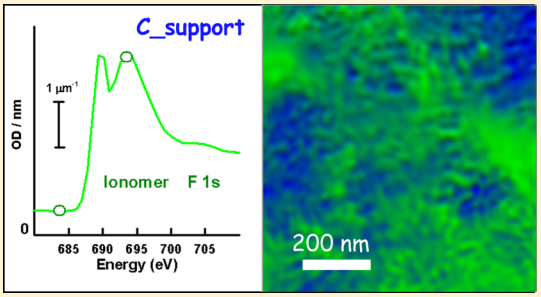


## 1. INTRODUCTION

Proton exchange membrane fuel cells (PEMFCs) are electrochemical devices, which convert chemical energy to electrical energy.[1] When hydrogen is used as the fuel, the only product is water. Because of their high energy conversion efficiency, high power density, rapid startup, and zero carbon emission,[1,2] PEMFCs are considered a desirable power conversion technology. They are currently under rapid development for automobile applications, with early introduction in selected markets by Toyota[3] and several other manufacturers.

A critical component in a PEMFC is the membrane electrode assembly (MEA), which consists of a proton-conducting membrane coated by anode and cathode catalyst layers (CLs).[4] The cathode CL is a porous structure composed of platinum nanocatalysts deposited on an electron-conducting carbon black support, a proton conductor, and open spaces for the transport of oxidant ($O_2$) and product ($H_2O$).[5,6] The most commonly used proton conductor in MEA electrodes is perfluorosulfonic acid (PFSA),[7] which has a high proton conductivity[8] and also acts as a binder to mechanically stabilize the CL.[6] Therefore, optimization of the spatial distribution of the PFSA ionomer in CLs relative to the active catalyst, support, and porosity can greatly improve platinum utilization, help to control gas permeability, and potentially achieve higher-temperature operation.[9] As with all such goals, the ability to optimize is closely related to the ability to visualize and quantitatively map the chemical components of interest.

However, despite great interest, quantitative imaging of ionomers in PEMFC CLs is poorly developed as it is rather challenging, mainly because of radiation damage issues. Although atomic force microscopy has been used to image the ionomer,[10,11] it can only provide information about surface topology.[12] Direct visualization of internal morphologies of ionomer with a few nanometer resolution has been claimed with transmission electron microscopy (TEM),[13] but there was no analytical verification. Typically, the view is that staining techniques are required,[14] but these may not be specific to ionomers and have the potential to modify the material. By targeting water as the signature, isolated hydrophilic domains (3−10 nm) have been observed by TEM in PFSA membranes.[15−17] In a recent study, Lopez-Haro et al.[18] visualized a $Cs^+$-stained ionomer layer deposited on a carbon black via three-dimensional (3D) TEM tomography. However, despite the high resolution and ability to access the 3D

Received: March 27, 2018
Revised: May 10, 2018
Published: May 10, 2018





DOI: 10.1021/acs.jpcc.8b02933
J. Phys. Chem. C 2018, 122, 11709−11719

structure, sample preparation challenges and radiation damage still greatly limit the application of TEM to ionomer materials.[14] Because of the high sensitivity of ionomers to radiation damage, electron beam irradiation causes mass loss, chemical transformation, and displacement of materials,[19−21] which introduces artifacts.[15]

Synchrotron-based scanning transmission X-ray microscopy (STXM) uses the intrinsic X-ray absorption spectral contrast to identify and quantitate chemical species with a spatial resolution of ∼30 nm.[22,23] STXM has significant advantages over analytical electron microscopy because of a lower rate of radiation damage relative to useful information obtained, as has been demonstrated in direct comparisons to both TEM−electron energy loss spectroscopy[24] and TEM−energy-dispersive X-ray spectroscopy.[20] Previously, STXM has been applied to track the changes of chemical constituents during fabrication of fuel cell electrode materials[25] and to quantitatively map ionomer distributions in activated CLs[26,27] and before and after a testing protocol that causes carbon corrosion.[28] Most PEMFC STXM studies to date have involved two-dimensional (2D) projection analysis. However, PEMFC CLs have a complex 3D structure. A proper understanding of CL structure and the impact on transport properties will only be achieved with 3D visualization methods. Hard X-ray tomography, using both laboratory[29] and synchrotron sources,[30,31] has been used very effectively for static and operando studies but is essentially blind to the low-molecular-weight, radiation-sensitive PFSA ionomer. We have been developing STXM spectro-tomography specifically for quantitative measurements of the 3D distribution of the PFSA ionomer in CLs. Berejnov et al.[32] and Wu et al.[21] have used room-temperature STXM spectro-tomography at the C 1s and F 1s edges to the 3D image ionomer in a PEMFC cathode. Other STXM spectro-tomography studies of PEMFC materials have been reported by Hitchcock and Toney,[33] Hitchcock,[23] and Schmid et al.[34] However, the morphological details and ionomer distributions in PEMFCs are still not well-resolved because of a combination of limited spatial resolution [∼30 nm, dictated by the zone plate (ZP) focusing optic] and the maximum sample thickness (∼300 nm) which is dictated by X-ray absorption at the F 1s edge.

Ptychography is a scanning coherent diffraction imaging (CDI) technique that can provide high spatial resolution imaging over large fields of view.[35−37] Unlike conventional X-ray imaging using ZPs (STXM, TXM, etc.), ptychography is not limited by image-forming optics and thus has the potential to reach the Rayleigh limit spatial resolution dictated by the wavelength of X-rays used.[38,39] Recently, soft X-ray ptychography has been developed by Shapiro et al.,[40] and ∼3 nm spatial resolution has been achieved using 1500 eV photons. Soft X-ray ptychography has been applied to magnetotactic bacteria,[41] catalyst particles,[42] lithium batteries,[43] calcium silicate hydrates,[44] and magnetic films.[45] The first soft X-ray spectro-ptycho-tomography has recently been reported.[46]

In this study, we report the use of soft X-ray spectro-ptychography to image 2D and 3D distributions of ionomers in PEMFC cathodes. Because ptychography relies on coherent scattering by sample components, there is a real question if noncrystalline soft matter such as the PFSA polymer can be successfully imaged with ptychography. We address this important question by performing ptychography on a model bilayer system consisting of one layer with isolated polytetrafluoroethylene (PTFE) fibers (mimicking PFSA) and a second layer containing Pt-coated crystalline graphitic fibers (mimicking the catalyst-coated carbon support).

At present, the radiation doses required for ptychographic imaging are typically much larger than those needed for conventional STXM, although one of the data sets reported in this work was measured using very low damage conditions. To track the damage with a view of evolving to minimal damage conditions as done with ambient temperature STXM spectro-tomography,[21] we have characterized the extent of damage caused by 2D and 3D imaging ptychographic imaging modalities. We also explore the spectroscopic information in ptychography which is richer than that in STXM because both phase and amplitude signals are acquired. In addition, ptychography-based spectro-tomography is used for 4D imaging—probing 3D distributions of ionomer in CLs—with the aim to better understand the organization of all components within PEMFC CLs.

## 2. EXPERIMENTAL SECTION

**2.1. Sample Preparation.** PEMFC catalyst-coated membrane (CCM) samples were cut into small rectangular pieces, embedded in an amine epoxy resin, and sectioned using a diamond blade ultramicrotome to a thickness of 100−300 nm. For the tomography measurements, a fresh scalpel was used to cut a single strip of the TEM Cu grid, which contained the CCM section of interest. When performing tomography measurements, the reduced width of the strip (∼150 $\mu$m) allows for sample rotation from −65° to 65° without hitting the order sorting aperture, which is a few hundred microns upstream of the focal point of the ZP.[34]

The model sample consisted of a two-layer polymer film with Pt-decorated graphitic carbon fibers embedded in an amine resin in one layer and PTFE (Teflon) fibers embedded in an amine resin in the second layer (see Figure 1). STXM tomography measurements on this sample have been presented earlier.[33,34]

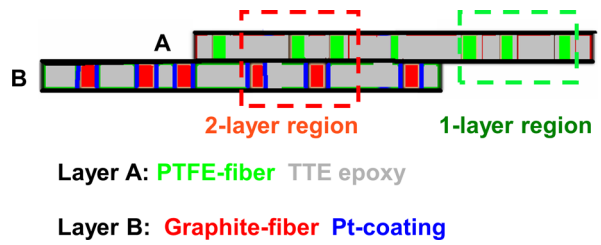


**Figure 1.** Cartoon of structure of the model sample used to evaluate the resolution improvement when using soft X-ray ptychography to measure noncrystalline soft matter. The dashed boxes indicate the type of areas measured for the data in Figure 2 (1-layer) and Figure 4 (2-layer).

**2.2. Data Collection.** STXM measurements were carried out using beamlines 11.0.2 and 5.3.2.1 at the Advanced Light Source (ALS), Lawrence Berkeley National Laboratory (LBNL). Instrumentation, STXM operational modes, and data analysis methods have been described in recent reviews.[22,47] Ptychographic measurements were performed using the STXM on the ALS 11.0.2 undulator beamline, modified by the addition of a Princeton Instruments direct-sense X-ray camera. Ptychography data sets were also obtained using a dedicated ptychography instrument, Nanosurveyor I,[48] on the ALS 5.3.2.1 bending magnet beamline. A ZP with an


DOI: 10.1021/acs.jpcc.8b02933
J. Phys. Chem. C 2018, 122, 11709−11719

Table 1. Summary of Conditions and Total Dose for Each Measurement Reported

| sample | BL—ZP $\delta_r$ | spot size (nm)[a] | dwell (ms) | thickness (nm) | OD 694 (eV) | $I_o$ (MHz) | Det. Eff. | # of images[b] | total dose (MGy)[c] | presented in figure |
|---|---|---|---|---|---|---|---|---|---|---|
| model, 1-layer | STXM—25 nm | 31 | 4 | 175 | 0.75 | 6.5 | 0.7 | 1 | 12 | 2a |
| model, 1-layer | 5321 ptycho—60 nm | 72 | 100 | 175 | 0.4 | 3.1 | 0.7 | 2 + 1 | 220 | 2b |
| model, 2-layer | 5321 ptycho—60 nm | 72 | 100 | 300 | 0.4 | 3.1 | 0.7 | 3 angles | 220 | 4 |
| MEA[d] | 11.0.2 STXM—60 nm | 72 | 1 | 130 | 1.2 | 9.5 | 0.4 | 2 | 4 | S2 |
| MEA | 11.0.2 ptycho—60 nm | 72 | 20 | 130 | 0.51 | 9.5 | 0.4 | 2 | 45 | 5 |
| MEA-11-GDE | 5321 STXM—60 nm | 72 | 2 | 230 | 1.05 | 1.7 | 0.7 | 74 | 14 | 6e |
| MEA-11-GDE | 5321 ptycho 2D—60 nm | 72 | 120 | 230 | (0.4)[e] | 2.5 | 0.7 | 33 | 280 | 6a–e |
| MEA-11-GDE | 5321 ptycho 3D—60 nm | 72 | 100 | 150 | 0.3@710 eV | 3.1 | 0.7 | 2 × (15 angles) = 30 | 320 | 7–9 |

[a]Cited spot size is the diffraction-limited spot expected for the ZP used (25 or 60 nm outer zone width). [b]Where two measurements were made, they were measured at 684 and 694 eV. Single measurements were made at 694 eV. [c]The total dose for the MEA sample was determined from the properties and exposure of the membrane to avoid the influence of Pt/carbon support. The excel program used for the dose calculation is provided in supplementary information of Wu et al.[21] [d]This MEA was provided by Ballard. The 25 $\mu$m wide, unreinforced, NRE-211 membrane had an equivalent weight of 1100. The cathode, which was fabricated by screen printing, had an ionomer/carbon mass ratio of 1.07 and a Pt loading of 0.65(4) mg/cm$^2$. The ionomer was Nafion-117. [e]OD of the sample was changing during the measurement because of fluorine loss. This is an estimate from the spectrum derived from the spectro-ptycho measurement (see Figure 5e).

outer zone width of 60 nm (100 nm) was used to illuminate the sample at beamline 11.0.2 (5.3.2.1). The sample is raster-scanned through the focal point with a step size of 50 nm. This makes the adjacent areas that are sampled overlap with each other, which is an important factor in achieving rapid convergence of the ptychography reconstruction. With the high brightness and coherence of the X-ray sources provided by the undulator at 11.0.2, a very short exposure time (20 ms) was sufficient to achieve good results. Despite this, the clock time to acquire ptychography data sets on beamline 11.0.2 was very long because of the ∼1 s readout time of the Princeton camera. At beamline 5.3.2.1, a custom, high-frame-rate CCD detector was used to record the diffraction data with single point exposure times of 100–200 ms. A silicon beam stop was used to avoid saturation of the bright-field signal at long dwell time, thereby increasing the dynamic range of the detector. At both 5.3.2.1 and 11.0.2 beamlines, the camera background signal was measured with the beamline shutter closed and removed in subsequent data processing.[40] Details of the measurements, along with estimates of the radiation dose used for each measurement, are given in Table 1. The doses were estimated using a simplified approach described in Wu et al.[21]

**2.3. Ptychography Reconstruction and Data Analysis.** Amplitude and phase images were derived from the measured ptychography diffraction patterns using 500 iterations of the relaxed averaged alternating reflection reconstruction algorithm implemented in the SHARP ptychography code[49] developed by the Center for Applied Mathematics for Energy Research Applications at Berkeley Lab. For spectroscopy data, each set of ptychographic amplitude images was combined into stacks and then aligned using Fourier cross-correlation routines in aXis2000.[50] The ptychographic amplitude signals were then converted to optical density (OD) signals using the ptychography amplitude signal in a region free of the sample but close to the sample region of interest (ROI). Ptychography OD signal from appropriate sets of image pixels was then extracted from the OD stacks and used for further analysis, such as generating chemical maps. Although we have not performed a detailed analysis of the phase signals, or the combined absorption and phase signals, as performed by Shapiro et al.,[40] one comparison of ionomer mapping by ptychographic absorption and by ptychographic phase is presented as supplementary information (see Figure S1).

**2.4. Ptycho-Tomography Acquisition and Data Analysis.** Ptychographic tomography measurements were performed using a piezo rotation stage, one of the key components of the Nanosurveyor-I instrument.[48] Eucentric alignment of the rotation axis with the ROI of the sample was achieved by iteratively adjusting the $x$ and $z$ axes of a piezo stage mounted on top of the rotation stage.[48] 2D coherent diffraction images were then recorded at a range of tilt angles (−57° to +69° with 9° steps). Higher tilt angles could not be achieved because of increasing sample thickness along the beam transmission direction. At each rotation angle, images were measured at 684 eV, below the F 1s onset, and at 710 eV, in the F 1s continuum. The two images were aligned. Maps of PFSA were generated by subtracting the pre-edge (684 eV) OD image from the post-edge (710 eV) OD image. Note that some of the STXM data used for comparative purposes were measured at 684 and 694 eV. While the signal magnitude is larger when the 694 eV signal is used, the fluorine maps are qualitatively similar to those measured at 710 eV. The effect of radiation damage for a given dose is also similar at the two energies because the signal decay rate ($d$OD/$d$(dose)) is similar at 694 and 710 eV. Absorption at 684 eV is dominated by the carbon support component. At the time of these measurements, it was not possible to measure ptychography signals at the C 1s edge. Thus, the chemical map of the carbon support ($C_{sup}$) was extracted by subtracting an appropriately weighted fraction of the PFSA map from the pre-edge image, according to

$$\mathrm{OD}_{C_{sup}} = \mathrm{OD}_{684} - a \times (\mathrm{OD}_{710} - \mathrm{OD}_{684}) \quad (1)$$

where $\mathrm{OD}_{C_{sup}}$ is the OD of the carbon support and $a$ is the ratio, $\mathrm{OD1}_{684}(\mathrm{PFSA})/\mathrm{OD1}_{684}(C_{sup})$, which is 0.21.[51] Here, OD1 refers to the OD of the component with a thickness of 1 nm. The chemical maps of PFSA and the carbon support at all tilt angles were then aligned in aXis2000 by Fourier correlation methods. The set of aligned chemical maps at all tilt angles was used to generate a 3D reconstruction using a compressed sensing (CS) algorithm[52,53] implemented in Mantis[54] (Mantis is available from http://spectromicroscopy.com). The 3D models of the two components were merged to generate a 4D model, which shows the quantitative distribution of both components in 3D. Visualization, segmentation, and analysis of the 3D data were performed using Avizo.[55]



DOI: 10.1021/acs.jpcc.8b02933
J. Phys. Chem. C 2018, 122, 11709–11719

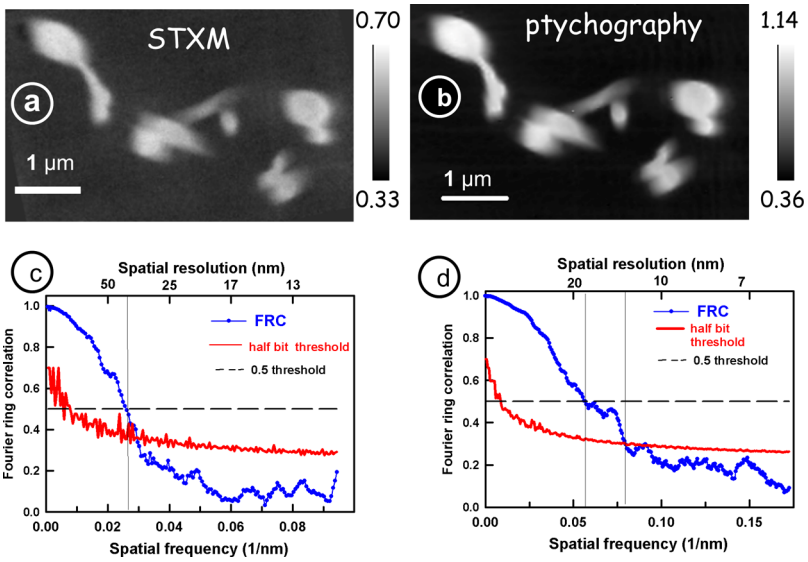


**Figure 2.** Images of the single layer region of the bilayer model sample (see Figure 1). (a) STXM OD image at 694 eV recorded with 1 ms/pixel sampling, using a ZP with 25 nm outer zone width (recorded after ptychography) (CLS 10ID1). (b) Ptychography absorption image at 694 eV of the same area. (c) FRC analysis of the spatial resolution for the STXM image of (a). (d) FRC analysis for the ptychography image of (b) (ALS 5.3.2.1).

**Table 2. Spatial Resolution of Ptychography and STXM Measurements**

| sample (microscope) | PTFE (CLS) | | PTFE (5.3.2.1) | | (PTFE, C, Pt) model (5.3.2.1) | | MEA (11.0.2) | | | MEA (5.3.2.1) |
|---|---|---|---|---|---|---|---|---|---|---|
| energy | | 694 eV | 694 eV | F-map | 694 eV | F map | 684 eV | 694 eV | F map | F 3d (*xy*) slice |
| method | TEM[a] | STXM[b] | ptycho | ptycho | ptycho | ptycho | ptycho | ptycho | ptycho | ptycho-tomo |
| ZP $\delta_r$ (nm)[a] | N/A | 25 | 60 | 60 | 60 | 60 | 60 | 60 | 60 | 60 |
| resolution (nm) (0.5 metric) | 5 | 35 | 18 | 13 | 9 | 15 | 16 | 13 | 13 | 23 |
| resolution (nm) (1/2-bit metric) | 4 | 33 | 13 | 11 | 10 | 12 | 14 | 12 | 12 | 20 |
| edge response (nm) 20−80% | 11 | 40 | 14 | 16 | 15 | 18 | 18 | 17 | 16 | 35 |

[a]Spatial resolution of a TEM image of a similar region as Figure 2a,b but without radiation damage from X-rays (see Figure 3). Note that the TEM used was operated under conditions where the instrumental resolution was 0.5 nm. [b]STXM with high-resolution ZP performed on the same area as measured by ptychography. See Figure 2. [c]Diffraction-limited resolution of a ZP is 1.22 × $\delta_r$, where $\delta_r$ is the width of the outer zone.

## 3. RESULTS

**3.1. Ptychography of the Model Sample.** To validate ptychography for imaging noncrystalline polymers such as PFSA, we measured a bilayer polymer model sample with the structure as shown in Figure 1. Region 1 (green rectangular box) is a single layer consisting of the PTFE fiber cross sections embedded in epoxy. Region 2 (red rectangular box) is two-layers, with the PTFE/epoxy layer on top of the layer containing cross sections of the platinum-coated graphitic fibers embedded in epoxy. Figure 2a shows a conventional STXM OD image at 694 eV of a microtomed cross section of several isolated PTFE fibers from region 1. This image was recorded at 694 eV using a ZP with 25 nm outermost zone width, which produces a theoretical diffraction-limited spot size of 31 nm. Figure 2b presents a ptychography absorption image of the same area measured at the same photon energy. Note that the ptychography amplitude image is recorded by serial sampling of the coherent scattering data with an exposure time of 100 ms at each pixel. Although PTFE is very radiation-sensitive, the morphologies of the PTFE fiber cross sections shown in the ptychography absorption image (Figure 2b) are similar to those in the conventional STXM image (Figure 2a) but with better spatial resolution. These figures indicate that 100 ms ptychographic exposure did not change the morphology of the PTFE fibers. Note that the STXM image was recorded AFTER the ptychography measurement so that the lower OD in the STXM image reflects fluorine loss caused by the ptychographic measurement.

To quantify the spatial resolution of the STXM and ptychography images, the Fourier ring correlation (FRC) method[56] was used, with results shown in Figure 2c,d. Single images were evaluated by splitting the image into an even and odd pixel set and measuring the correlation between them, and the associated 2$\sigma$, according to the formulae given by Saxton and Baumeister.[57] The spatial resolution estimates for all of the model bilayer and MEA measurements are summarized in Table 2. For the STXM image in Figure 2a, the intersection of the FRC curve (blue, Figure 2c) and both the 0.5 threshold line (dashed gray line, Figure 2c) and the 1/2-bit curve occur at 0.028 $nm^{-1}$, which indicates a spatial resolution of 35 nm, consistent with near diffraction-limited performance of the ZP used. The FRC curve of the ptychography image (blue, Figure 2d) drops below the threshold line of 0.5 (dashed gray line, Figure 2d) at a spatial frequency of 0.056 $nm^{-1}$, which corresponds to a spatial resolution of 18 nm, and crosses the 1/2-bit curve at 0.078 $nm^{-1}$, which corresponds to a spatial resolution of 13 nm. Sub-10 nm spatial resolution has been achieved previously with soft X-ray ptychography.[40,41] The spatial resolution of ∼15 nm achieved by ptychography on a soft matter sample is impressive considering that (i) the 5.3.2.1



DOI: 10.1021/acs.jpcc.8b02933
J. Phys. Chem. C 2018, 122, 11709−11719

bend magnet beamline has a relatively low coherent fraction compared to that of the 11.0.2 undulator beamline, where the highest resolution data were obtained,[38,40] and (ii) this is a soft matter polymer sample, which has a very weak coherent scattering signal.

One can speculate that spatial resolution is affected not only by the ability of soft X-ray ptychography to image soft matter but also by the intrinsic properties of the sample, in particular by the abruptness of the PTFE/epoxy interface. To investigate this possibility, the bilayer polymer model sample was imaged using TEM. Figure 3a shows a TEM image of the similar region

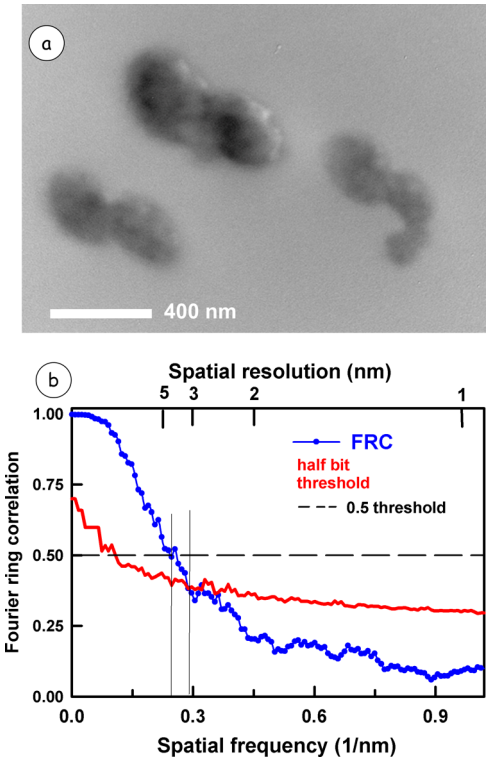


**Figure 3.** (a) TEM image of a fresh area of the PTFE single layer of the bilayer sample (bright field, 100 keV). (b) FRC analysis of spatial resolution of the TEM image, verifying that the edges of the PTFE fibers are sharp at a spatial scale significantly lower than that measured by ptychography.

but without exposure to any X-rays. It shows that the abruptness of the epoxy−PTFE interface is considerably below 5 nm (Figure 3b), indicating that the intrinsic sharpness of the fiber edges is not limiting the resolution achievable by ptychography. The ∼15 nm spatial resolution of ptychography of PTFE fibers (Figure 2b) achieved with a 60 nm ZP is clearly better than that obtained using conventional STXM with a 25 nm ZP (Figure 2a). This is experimental evidence that ptychography can improve the spatial resolution when applied to soft matter samples.

Figure 4a shows a conventional STXM transmission image of region 2 of the two-layer model sample (see Figure 1), recorded at 694 eV using a 60 nm ZP. Figure 4b is the ptychography absorption image of the same region recorded at 694 eV. Figure 4c is a ptychography absorption image of this region at 684 eV below the onset of F 1s absorption. Two different morphologies are apparent in Figure 4b: one has an irregular polygon shape (indicated by yellow arrows) and the other is fuzzy with a spiral shape (indicated by red arrows).

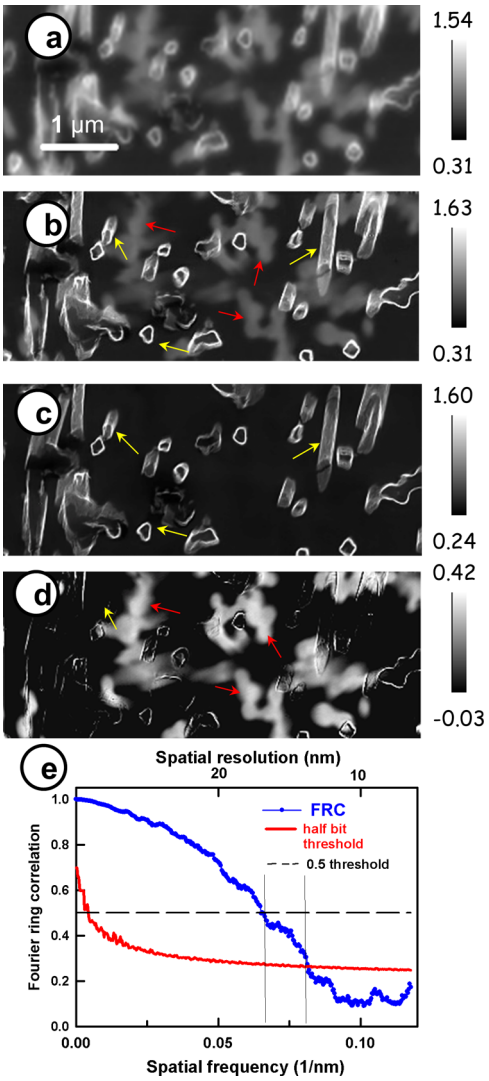


**Figure 4.** Images of the two-layer region of the bilayer model sample (see Figure 1). (a) STXM transmission image at 694 eV recorded using a ZP with 60 nm outer zone width. Ptychography absorption images at (b) 684 and (c) 694 eV. (d) Fluorine map obtained by taking the difference between ptychography absorption images at 694 eV (Figure 3b) and 684 eV (Figure 3c). (e) FRC analysis of spatial resolution of the ptychography fluorine map. The OD is indicated by a grayscale bar for each image. Yellow and red arrows denote the Pt shells and PTFE fibers, respectively (ALS, 5.3.2.1).

However, the pre-edge image (Figure 4c) only shows the irregular polygon shapes that are the platinum-coated graphite fibers which absorb at all X-ray energies. The lower contrast spiral-shaped structures are cross sections of the PTFE fibers because they are only observed at energies above the F 1s onset. Figure 4d is the difference between the two ptychographic absorption images at 694 eV (Figure 4b) and 684 eV (Figure 4c), which is a map of the fluorine, and thus the PTFE fibers in this region of the sample. Figure 4d also shows some residual signal at the edges of the Pt-coated graphite fibers, which probably is related to imperfect alignment. Figure 4e displays the FRC analysis of the fluorine map in Figure 4d. This analysis indicates a spatial resolution of 15 nm based on the 0.5 threshold or 12 nm based on the 1/2-bit threshold. Figures 2 and 4 clearly demonstrate that soft X-ray ptychography is capable of chemically imaging radiation-sensitive soft materials



DOI: 10.1021/acs.jpcc.8b02933
J. Phys. Chem. C 2018, 122, 11709−11719

with a spatial resolution higher than that provided by conventional STXM. Because PTFE and PFSA have similar radiation damage rates,[19] this model sample study indicates that ptychography is able to characterize the distribution of PFSA in real fuel cell samples.

**3.2. Spectro-Ptychography of an MEA CL.** Figure S2 presents a STXM OD image at 694 eV (recorded with a 60 nm outer zone ZP) of the cathode region of an MEA. It consists of three regions: embedding epoxy (TTE, left), cathode CL (middle), and membrane (right). Because of the low-resolution ZP used (60 nm outer zone width, thus 72 nm diffraction-limited resolution), the morphology and structure of the cathode are poorly resolved in the conventional STXM image. Figure 5a,b shows ptychography absorption images at 684 and 694 eV, measured at the ALS 11.0.2 undulator beamline, of the rectangular region indicated in Figure S2. Figure 5c is the difference between Figure 5b and a, which maps the fluorine signal from PFSA in both the CL and the membrane. Note that the dark regions in the fluorine map (Figure 5c) correspond to the bright regions in Figure 5a, which are carbon-rich. The PFSA ionomer in the CL (Figure 5c) has a "feather"-like morphology, illustrated by the region in the purple dashed rectangle in Figure 5b,c. Figure 5d is a color-coded composite of the F-map and the carbon support, with the latter derived from the pre-F 1s image and the F-map (carbon support = $OD_{684}$ − 0.21 × F-map).

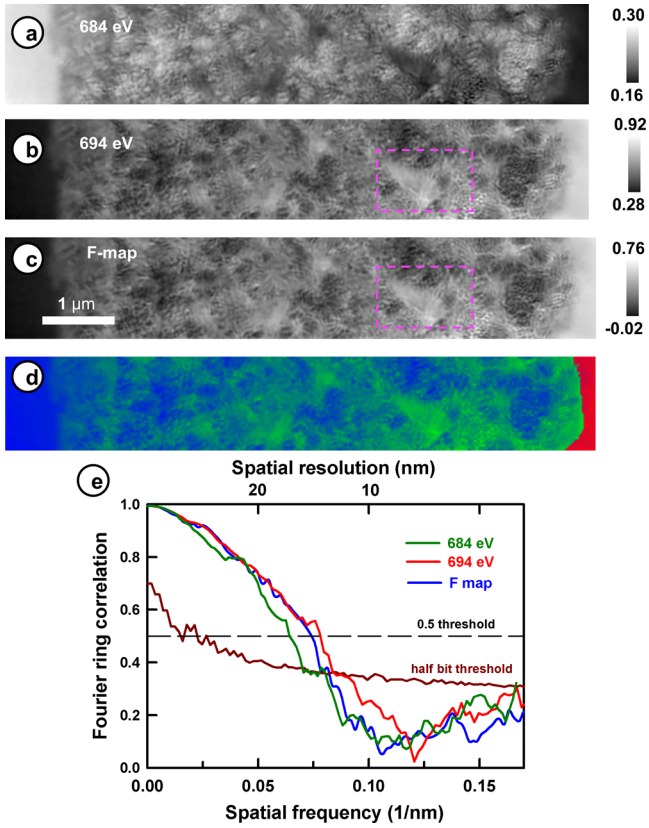


**Figure 5.** Ptychography absorption images of the MEA cathode (white rectangle in STXM image shown in Figure S3) (a) at 684 eV and (b) at 694 eV. (c) Fluorine map, image difference OD(694 eV) − OD(684 eV). (d) Color-coded composite of the membrane (red), ionomer (green), and carbon (support and epoxy) (blue). The membrane and ionomer maps are threshold masked extracts of the fluorine map. (Note that although the PFSA of the membrane and the PFSA of the ionomer are differentiated based on the signal intensity in this study, the membrane and cathode PFSA can be chemically different, leading to detectable differences in their C 1s and F 1s spectra.[51]) The carbon signal is derived from the image at 684 eV. (e) FRC analysis of the fluorine map (c). The OD is indicated by the grayscale bar at the right side of each image (ALS, 11.0.2).

The results of FRC analysis of the ptychography absorption images at 684 and 694 eV and the F 1s map are presented in Figure 5e. Table 2 summarizes the spatial resolution of these three images evaluated using the 1/2-bit and 0.5 threshold criteria, along with a visual estimate of the resolution derived from 20 to 80% intensity jumps at sharp interfaces. Generally, the spatial resolution determined with the 0.5 threshold is lower than that with the 1/2-bit threshold. At 684 eV, the resolution (mean of the two FRC criteria) is 15 ± 1 nm, while it is 13 ± 1 nm at 694 eV and for the fluorine map (PFSA). The resolution achieved for the fuel cell cathode is slightly improved relative to that achieved for the model sample, consistent with the stronger scattering ability of the Pt-coated carbon support particles.

A full stack[58] acquisition (33 energies from 681 to 710 eV) was also measured to explore spectro-ptychography of the CL at the F 1s edge. This provides a high-resolution probe of both the spectroscopy[51] and spatial distribution of the PFSA ionomer in a real cathode CL sample. After reconstructing the ptychographic data for each image and converting the amplitude signal to absorption, the set of 33 OD images was aligned. The aligned stack was then processed using singular value decomposition (SVD)[59] to derive maps of the PFSA and the non-F-containing components. Figure 6 presents the component maps of the whole PFSA component (Figure 6a) including both the membrane and cathode, the map of only ionomer in cathode (PFSA in the CL, derived by threshold masking and subtracting the membrane signal) (Figure 6b), and the map of nonfluorinated components (Pt-decorated carbon support) (Figure 6c). Figure 6d is a rescaled color composite of the membrane (red), ionomer (green), and carbon support (blue) component maps. Each spot was measured for a total time of ~4 s (33 × 0.12 s) corresponding to an estimated total dose of 280 MGy. Because this is approximately 7 times higher than the critical dose for PFSA damage,[19] PFSA was extensively damaged during the spectro-ptychography measurement. Figure 6e shows the F 1s spectrum of the membrane as measured by STXM after spectro-ptychography (red), compared to that measured prior to the spectro-ptychography (green), in both cases using a 1 ms/pixel dwell time which causes negligible damage. The ptychography data acquisition transforms the characteristic two-peak F 1s spectrum of undamaged PFSA (green in Figure 6e) into a single, broad, asymmetric peak. That change and the reduced F 1s continuum signal indicate a significant reduction of the total fluorine content in the PFSA component. As expected from other studies of radiation damage to PFSA,[19,21] the spectrum, and thus the chemical structure, is significantly modified by the high X-ray dose used to perform spectro-ptychography. The F 1s edge jump ($OD_{710}$ − $OD_{684}$) after is less than a quarter of that before the spectro-ptychography measurement, indicating that a significant amount of the PFSA has been lost and the remaining fluorine-containing material has been chemically modified. The dashed line in Figure 6e shows that the peak of the F 1s signal after ptychography is at an energy between those of the two peaks of undamaged PFSA, consistent with a disordered system without the well-defined $-(CF_2-CF_2)_n-$


DOI: 10.1021/acs.jpcc.8b02933
J. Phys. Chem. C 2018, 122, 11709−11719

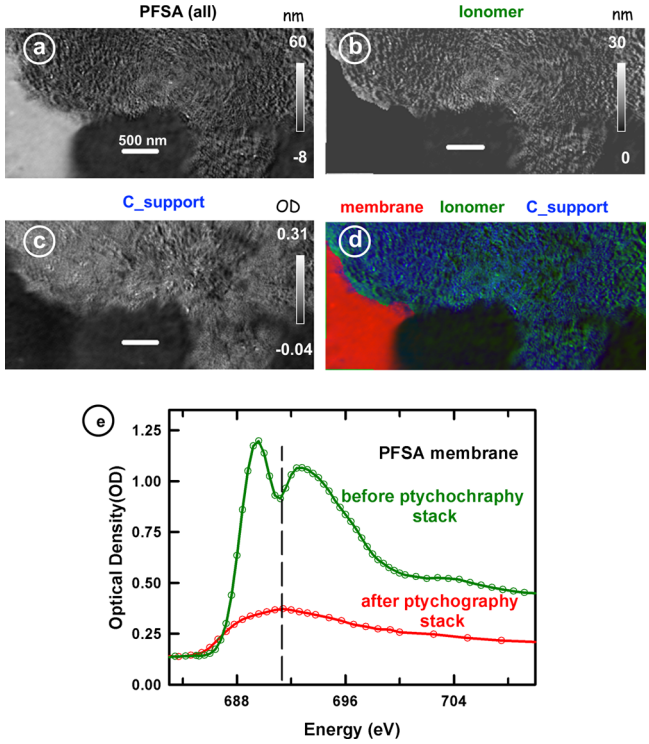


**Figure 6.** Ptychography F 1s edge full stack (33 energy points) of the fuel cell cathode CL, analyzed using a two-component SVD fit. (a) PFSA component map. (b) Ionomer map in the cathode region only, derived by subtracting the threshold masked membrane signal. (c) Map of nonfluorine components (mainly carbon support). (d) Color-coded composite of component maps of membrane (red), ionomer (green), and carbon support (blue). (e) F 1s spectra of the membrane region recorded before (green) and after (red) ptychography by low-dose (2 ms dwell) STXM. The dashed line indicates the position of the peak of the F 1s signal after the sample was damaged by the ptychography measurement. The intensity scales in (a,b) are nanometer thickness, based on a fit to the F 1s ptychography spectrum displayed in part (e) divided by 60 to match the F 1s continuum of the OD1 spectrum of undamaged PFSA. The intensity scale for (c) is the OD of the constant signal (ALS, 5.3.2.1).

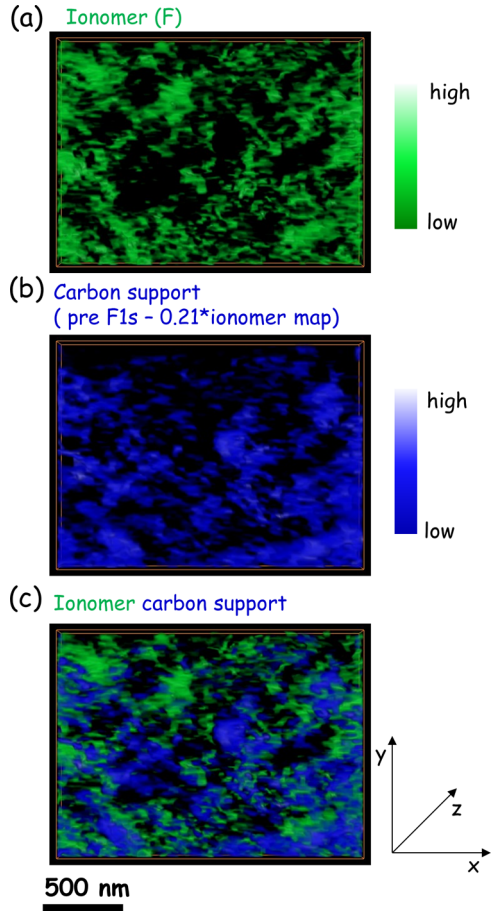


**Figure 7.** 4D imaging of the fuel cell cathode CL. Volume renderings of the 3D chemical structure of the cathode derived from a CS tomographic reconstruction of two-energy F 1s spectro-ptycho-tomography data. (a) Ionomer. (b) Carbon support. Threshold values for these renderings are 0.0023 for ionomer and 0.0031 for carbon support. (c) Color composite (ionomer in green, carbon support in blue) (ALS, 5.3.2.1).

regions which give rise to the characteristic F 1s → $\sigma^*_{C-F}$ (⊥) and F 1s → $\sigma^*_{C-F}$ (∥) transitions at 690 and 694 eV.[50] Here, $\sigma^*_{C-F}$ (⊥) and $\sigma^*_{C-F}$ (∥) refer to electronic bands aligned along and perpendicular to the C−C chain. The chemical structure of PFSA after high-dose X-ray damage is known to be able to resist further structural modifications.[20] The calculated radiation dose for the ptychography measurement at beamline 11.0.2 (results shown in Figure 5) is 45 MGy. This is similar to the critical dose for radiation damage to PFSA[19] and will have caused about 50% fluorine loss.[21] For the measurements using beamline 5.3.2.1 (Figures 6−8), the total dose was much larger. However, we find that after ∼120 MGy, the fluorine loss rate slows considerably, and the remaining modified fluoropolymer is more stable.

**3.3. Ptychographic Imaging: Two-Energy Ptycho-Tomography of Ionomers.** A PEMFC MEA sample with a thickness of ∼150 nm was measured by two-energy F 1s ptychographic tomography. The tilt angle range was −57° to +69° with 9° increment. After alignment, conversion to OD, and generation of component maps for the ionomer and the carbon support at each tilt angle, the set of component maps at the 14 tilt angles was aligned and then reconstructed using the CS method implemented in Mantis.[53] A $\beta$ value of 0.1 and 50 iterations were used in the CS reconstruction. Figure 7 presents volume-rendered visualizations of the PEMFC cathode CL based on the ptychographic tomography F 1s stack maps. Figure 7a,b is 3D volume renderings of the ionomer (green, based on an Otsu threshold[60] of 0.0023) and carbon support (blue, based on an Otsu threshold of 0.0031), on relative color scales, while Figure 7c is a 4D image, that is, a volume rendering of the color composite of the two component volumes. Figure 8 shows three sets of color-coded composite slices in the *yz* (Figure 8a−c), *xz* (Figure 8d−f), and *xy* (Figure 8h−j) planes, which are sliced through the 3D volume at the planes indicated in Figure 8g. The volume fraction of the ionomer is 28%, and the volume fraction of the carbon support is 43%. There is significant overlap of these volume elements because of the finite spatial resolution and reconstruction uncertainty. The total solid fraction of the summed ionomer and carbon support volumes is 57%. Thus, the estimated porosity of the volume is 43%. The average thicknesses of the carbon support particles and PFSA strands are 40 and 22 nm, respectively. The carbon support component typically consists of agglomerations of ∼50 nm diameter carbon black particles. The ionomer is believed to form a less than 10 nm thick conformal layer on carbon particles decorated with the Pt



DOI: 10.1021/acs.jpcc.8b02933
J. Phys. Chem. C 2018, 122, 11709−11719

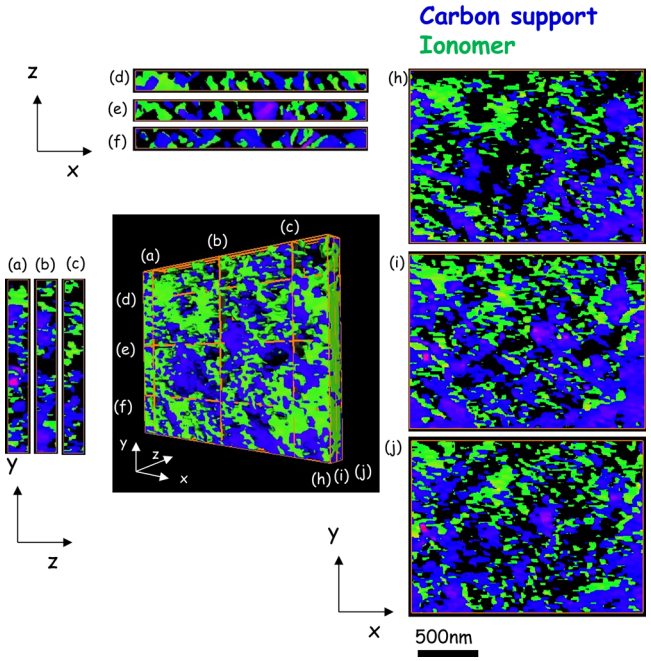


**Figure 8.** Multiple slices from the 3D rendered volume of the two components derived from F 1s spectro-ptycho-tomography. (a–c) In *zy* plane, (d–f) in *xz* plane, and (h–j) in *xy* plane. (g) indicates the position of each slice in the volume image. Threshold values for the slices are 0.0031 for the ionomer and 0.0023 for the carbon support. See Supporting Information for a movie with a detailed rendering and display of this 4D reconstruction (ALS, 5.3.2.1).

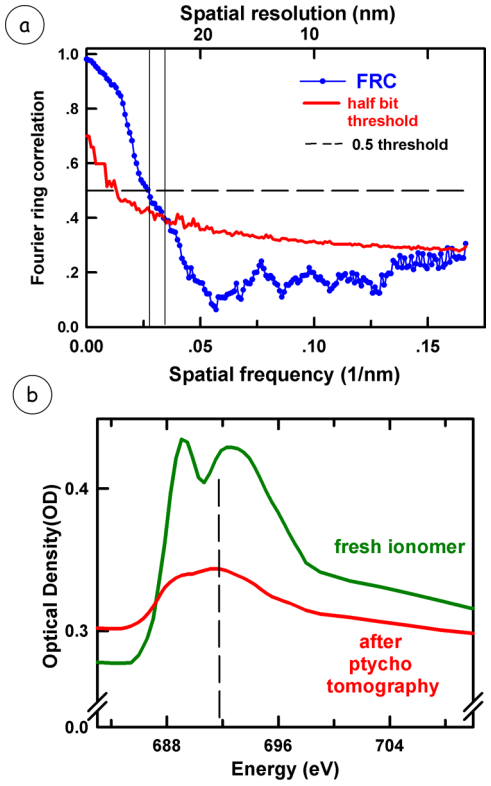


**Figure 9.** (a) FRC analysis of an *yz* slice of the 3D reconstruction of the ptycho-tomography PFSA component signal (Figure 8). (b) F 1s spectra of the cathode region extracted from a F 1s stack recorded by conventional STXM after the spectro-ptycho-tomography measurement. The spectrum of the area where ptycho-tomography was performed is in red, while the spectrum of fresh ionomer is in green. The dashed line indicates the position of the peak of the F 1s signal after ptychography (ALS, 5.3.2.1).

catalyst, but there is no definitive knowledge. Different CL formulation and processing affect both carbon support and ionomer components, resulting in different 4D distributions.[27] The spatial resolution of the spectro-ptycho-tomographic 4D imaging (component maps presented in Figure 7) is estimated to be 28 ± 9 nm (Figure 9a, Table 2), as evaluated by applying FRC to several different *yz* slices.

The F 1s spectrum of PFSA in the cathode after the spectro-ptycho-tomography measurement is shown in Figure 9b (red), compared to the spectrum from a fresh area of ionomer (green). The estimated total radiation dose used to perform the measurement was 320 MGy. At this high radiation dose, the two-peak spectral structure of undamaged PFSA was fully converted to a single peak and there was extensive fluorine loss. The increased pre-F 1s-edge signal indicates that there was also a significant carbon buildup during the measurement.

## 4. DISCUSSION

This study shows that the spatial resolution of X-ray imaging of soft materials such as PTFE and PFSA can be improved by soft X-ray ptychography. Chemically specific imaging with spectro-ptychography was achieved (Figures 5 and 6), a capability demonstrated in earlier measurements.[41,61] The measurements at 11.0.2 beamline (Figure 5) exposed each pixel to only ∼40 ms of X-ray beam. Because the ptychography imaging was performed with a larger beam diameter (70 nm rather than 30 nm), the ∼40 ms exposure corresponds to ∼10 ms of conventional STXM, an exposure which does minimal damage. Thus, even with the soft X-ray ptychography system used in this work, it was possible to obtain a scientifically valid high-resolution analysis of ionomers in a cathode CL. One limitation is that a direct-detect X-ray camera for photon energies below ∼500 eV does not exist yet. For best quality 4D imaging of cathodes, it is better to explicitly measure a spectral signal specific to the carbon support, which is usually determined from the difference of OD images measured at 285.1 eV (C 1s → $\pi^*$ transition of the graphitic support) and 278 eV (pre-C 1s, dominated by Pt and F).[26,27]

The improved spatial resolution and thus the potential of spectro-ptycho-tomography for 3D mapping ionomers in PEMFC cathodes were clearly demonstrated (Figures 7–9). As compared to conventional soft X-ray STXM tomography,[21,53] the higher spatial resolution means there are more differentiable layers of signal in the *z*-direction (Figure 8). If the dose can be decreased, which seems feasible with a brighter source and thus larger coherence, then room-temperature 3D chemical imaging by spectro-ptycho-tomography will provide 3D ionomer maps, which can help PEM-FC CL optimization. Further improvements are possible if ptychography is performed at cryogenic temperatures to reduce the physical loss of fluorine. A new STXM with cryo-tomography capabilities for both STXM and ptychography has recently been developed at the Canadian Light Source.[62]

## 5. CONCLUSIONS

Spectroscopic scanning CDI (spectro-ptychography) was used to image PFSA ionomers in PEMFC cathodes with a 2D spatial resolution better than 15 nm and a 3D spatial resolution better than 30 nm. At present, full spectro-ptychography and spectro-


DOI: 10.1021/acs.jpcc.8b02933
J. Phys. Chem. C 2018, 122, 11709–11719

ptycho-tomography require doses that cause significant radiation damage. However, improved instrumentation, such as the recently commissioned COSMIC[63] system at ALS, will reduce the dose required to the point where highly radiation-sensitive soft matter samples, such as PFSA ionomer, can be measured with an acceptable level of chemical and structural modification using few-energy spectro-ptychography mapping and few-tilt-angle spectro-ptycho-tomography.

## ■ ASSOCIATED CONTENT

### Supporting Information

The Supporting Information is available free of charge on the ACS Publications website at DOI: 10.1021/acs.jpcc.8b02933.

Ptychography absorption difference compared to ptychography phase difference and STXM OD image of the same region of the sample measured by ptychography (PDF)

Color-coded combination of the renderings of the 3D reconstruction of the carbon support and ionomer derived from spectro-ptychographic tomography (MPG)

## ■ AUTHOR INFORMATION


### Corresponding Author

*E-mail: aph@mcmaster.ca.

### ORCID

Adam P. Hitchcock: 0000-0002-1598-7886


### Notes

The authors declare no competing financial interest.

The data that support the findings of this study are available from the corresponding authors upon reasonable request.

## ■ ACKNOWLEDGMENTS

We thank Mirna Lerotic (2nd Look consulting), who wrote the CS tomography software. Pytchography and STXM data were measured at beamlines 11.0.2 and 5.3.2.1 at the Advanced Light Source, which is supported by the Director of the Office of Science, Department of Energy, under contract no. DE-AC02-05CH11231. Some STXM data were also measured at the ambient STXM on the Canadian Light Source (CLS) beamline 10ID1. The CLS is supported by the Canadian Foundation for Innovation. Ptychography data analysis was performed using SHARP, which is supported by the Center for Applied Mathematics for Energy Research Applications (CAMERA), a partnership between Basic Energy Sciences (BES) and Advanced Scientific Computing Research (ASRC) at the US Department of Energy.

## ■ REFERENCES


(1) Wang, Y.; Chen, K. S.; Mishler, J.; Cho, S. C.; Adroher, X. C. A Review of Polymer Electrolyte Membrane Fuel Cells: Technology, Applications, and Needs on Fundamental Research. *Appl. Energy* **2011**, *88*, 981−1007.

(2) Gwak, G.; Ju, H. A Rapid Start-up Strategy for Polymer Electrolyte Fuel Cells at Subzero Temperatures Based on Control of the Operating Current Density. *Int. J. Hydrogen Energy* **2015**, *40*, 11989−11997.

(3) Yoshida, T.; Kojima, K. Toyota MIRAI Fuel Cell Vehicle and Progress Toward a Future Hydrogen Society. *Interface Mag.* **2015**, *24*, 45−49.

(4) Ji, M.; Wei, Z. A Review of Water Management in Polymer Electrolyte Membrane Fuel Cells. *Energies* **2009**, *2*, 1057−1106.

(5) Xie, J.; Xu, F.; Wood, D. L.; More, K. L.; Zawodzinski, T. A.; Smith, W. H. Influence of Ionomer Content on the Structure and Performance of PEFC Membrane Electrode Assemblies. *Electrochim. Acta* **2010**, *55*, 7404−7412.

(6) Eguchi, M.; Baba, K.; Onuma, T.; Yoshida, K.; Iwasawa, K.; Kobayashi, Y.; Uno, K.; Komatsu, K.; Kobori, M.; Nishitani-Gamo, M.; et al. Influence of Ionomer/carbon Ratio on the Performance of a Polymer Electrolyte Fuel Cell. *Polymers* **2012**, *4*, 1645−1656.

(7) Gottesfeld, S.; Zawodzinski, T. A. *PFSA-Book. In Advances in Electrochemical Science and Engineering*; Alkire, R. C., Gerischer, H., Kolb, D. M., Tobias, C. W., Eds.; Wiley-VCH: Weinheim, Germany, 1997; p 195.

(8) Li, Q.; He, R.; Jensen, J. O.; Bjerrum, N. Approaches and Recent Development of Polymer Electrolyte Membranes for Fuel Cells Operating above 100 C. *Chem. Mater.* **2003**, *15*, 4896−4915.

(9) Holdcroft, S. Fuel Cell Catalyst Layers: A Polymer Science Perspective. *Chem. Mater.* **2013**, *26*, 381−393.

(10) He, Q.; Kusoglu, A.; Lucas, I. T.; Clark, K.; Weber, A. Z.; Kostecki, R. Correlating Humidity-Dependent Ionically Conductive Surface Area with Transport Phenomena in Proton-Exchange Membranes. *J. Phys. Chem. B* **2011**, *115*, 11650−11657.

(11) Bass, M.; Berman, A.; Singh, A.; Konovalov, O.; Freger, V. Surface Structure of Nafion in Vapor and Liquid. *J. Phys. Chem. B* **2010**, *114*, 3784−3790.

(12) Allen, F. I.; Comolli, L. R.; Kusoglu, A.; Modestino, M. A.; Minor, A. M.; Weber, A. Z. Morphology of Hydrated as-Cast Nafion Revealed Through Cryo Electron Tomography. *ACS Macro Lett.* **2015**, *4*, 1−5.

(13) More, K.; Reeves, S. TEM Specimen Preparation of Partially-Embedded Electrodes From Proton Exchange Membrane Fuel Cell Membrane Electrode Assemblies. *Microsc. Microanal.* **2005**, *11*, 2104−2105.

(14) Kusoglu, A.; Weber, A. Z. New Insights into Perfluorinated Sulfonic-Acid Ionomers. *Chem. Rev.* **2017**, *117*, 987−1104.

(15) Yakovlev, S.; Balsara, N. P.; Downing, K. H. Insights on the Study of Nafion Nanoscale Morphology by Transmission Electron Microscopy. *Membranes* **2013**, *3*, 424−439.

(16) Wang, C.; Krishnan, V.; Wu, D.; Bledsoe, R.; Paddison, S. J.; Duscher, G. Evaluation of the Microstructure of Dry and Hydrated Perfluorosulfonic Acid Ionomers: Microscopy and Simulations. *J. Mater. Chem. A* **2013**, *1*, 938−944.

(17) Lin, J.; Wu, P.-H.; Wycisk, R.; Pintauro, P. N.; Shi, Z. Properties of Water in Prestretched Recast Nafion. *Macromolecules* **2008**, *41*, 4284−4289.

(18) Lopez-Haro, M.; Guétaz, L.; Printemps, T.; Morin, A.; Escribano, S.; Jouneau, P.-H.; Bayle-Guillemaud, P.; Chandezon, F.; Gebel, G. Three-Dimensional Analysis of Nafion Layers in Fuel Cell Electrodes. *Nat. Commun.* **2014**, *5*, 5229.

(19) Melo, L. G. A.; Botton, G. A.; Hitchcock, A. P. Quantification of the Critical Dose for Radiation Damage to Perfluorosulfonic Acid Membranes Using Soft X-Ray Microscopy. *Microsc. Microanal.* **2015**, *21*, 2443−2444.

(20) Melo, L. G. d. A.; Hitchcock, A. P.; Jankovic, J.; Stumper, J.; Susac, D.; Berejnov, V. Quantitative Mapping of Ionomer in Catalyst Layers by Electron and X-Ray Spectromicroscopy. *ECS Trans.* **2017**, *80*, 275−282.

(21) Wu, J.; Melo, L. G. A.; Zhu, X.; West, M. M.; Berejnov, V.; Susac, D.; Stumper, J.; Hitchcock, A. P. 4D Imaging of Polymer Electrolyte Membrane Fuel Cell Catalyst Layers by Soft X-Ray Spectro-Tomography. *J. Power Sources* **2018**, *381*, 72−83.

(22) Hitchcock, A. P. Soft X-Ray Imaging and Spectromicroscopy. In *Handbook of Nanoscopy*; Van Tendeloo, G., Van Dyck, D., Pennycook, J. S., Eds.; Wiley, 2012; *Vol. II*, pp 745−792.

(23) Hitchcock, A. P. Soft X-Ray Spectromicroscopy and Ptychography. *J. Electron Spectrosc. Relat. Phenom.* **2015**, *200*, 49−63.

(24) Wang, J.; Botton, G. A.; West, M. M.; Hitchcock, A. P. Quantitative Evaluation of Radiation Damage to Polyethylene Terephthalate by Soft X-Rays and High-Energy Electrons. *J. Phys. Chem. B* **2009**, *113*, 1869−1876.

(25) Lee, V.; Berejnov, V.; West, M.; Kundu, S.; Susac, D.; Stumper, J.; Atanasoski, R. T.; Debe, M.; Hitchcock, A. P. Scanning Transmission X-Ray Microscopy of Nano Structured Thin Fi Lm Catalysts for Proton-Exchange-Membrane Fuel Cells. *J. Power Sources* **2014**, *263*, 163−174.
(26) Susac, D.; Berejnov, V.; Hitchcock, A. P.; Stumper, J. STXM Study of the Ionomer Distribution in the PEM Fuel Cell Catalyst Layers. *ECS Trans.* **2011**, *41*, 629−635.
(27) Susac, D.; Berejnov, V.; Hitchcock, A. P.; Stumper, J. STXM Characterization of PEM Fuel Cell Catalyst Layers. *ECS Trans.* **2012**, *50*, 405−413.
(28) Hitchcock, A. P.; Berejnov, V.; Lee, V.; West, M.; Colbow, V.; Dutta, M.; Wessel, S. Carbon Corrosion of Proton Exchange Membrane Fuel Cell Catalyst Layers Studied by Scanning Transmission X-Ray Microscopy. *J. Power Sources* **2014**, *266*, 66−78.
(29) Epting, W. K.; Gelb, J.; Litster, S. Resolving the Three-Dimensional Microstructure of Polymer Electrolyte Fuel Cell Electrodes Using Nanometer-Scale X-Ray Computed Tomography. *Adv. Funct. Mater.* **2012**, *22*, 555−560.
(30) Schneider, A.; Wieser, C.; Roth, J.; Helfen, L. Impact of Synchrotron Radiation on Fuel Cell Operation in Imaging Experiments. *J. Power Sources* **2010**, *195*, 6349−6355.
(31) Eller, J.; Marone, F.; Büchi, F. N. Operando Sub-Second Tomographic Imaging of Water in PEFC Gas Diffusion Layers. *ECS Trans.* **2015**, *69*, 523−531.
(32) Berejnov, V.; Susac, D.; Stumper, J.; Hitchcock, A. P. 3D Chemical Mapping of PEM Fuel Cell Cathodes by Scanning Transmission Soft X-Ray Spectrotomography. *ECS Trans.* **2013**, *50*, 361−368.
(33) Hitchcock, A. P.; Toney, M. F. Spectromicroscopy and Coherent Diffraction Imaging: Focus on Energy Materials Applications. *J. Synchrotron Radiat.* **2014**, *21*, 1019−1030.
(34) Schmid, G.; Obst, M.; Wu, J.; Hitchcock, A.. 3D Chemical Imaging of Nanoscale Biological, Environmental, and Synthetic Materials by Soft X-Ray STXM Spectrotomography. In *X-ray and Neutron Techniques for Nanomaterials Characterization*; Kumar, C. S. S. R., Ed.; Springer: Berlin, 2016; pp 43−94.
(35) Thibault, P.; Guizar-Sicairos, M.; Menzel, A. Coherent Imaging at the Diffraction Limit. *J. Synchrotron Radiat.* **2014**, *21*, 1011−1018.
(36) Rodenburg, J. M.; Faulkner, H. M. L. A Phase Retrieval Algorithm for Shifting Illumination. *Appl. Phys. Lett.* **2004**, *85*, 4795−4797.
(37) Pfeiffer, F. X-Ray Ptychography. *Nat. Photonics* **2018**, *12*, 9−17.
(38) Miao, J.; Ishikawa, T.; Robinson, I. K.; Murnane, M. M. Beyond Crystallography: Diffractive Imaging Using Coherent X-Ray Light Sources. *Science* **2015**, *348*, 530−535.
(39) Edo, T. B.; Batey, D. J.; Maiden, A. M.; Rau, C.; Wagner, U.; Pešić, Z. D.; Waigh, T. A.; Rodenburg, J. M. Sampling in X-Ray Ptychography. *Phys. Rev. A: At., Mol., Opt. Phys.* **2013**, *87*, 053850.
(40) Shapiro, D. A.; Yu, Y.-S.; Tyliszczak, T.; Cabana, J.; Celestre, R.; Chao, W.; Kaznatcheev, K.; Kilcoyne, A. L. D.; Maia, F.; Marchesini, S.; et al. Chemical Composition Mapping with Nanometre Resolution by Soft X-Ray Microscopy. *Nat. Photonics* **2014**, *8*, 765−769.
(41) Zhu, X.; Hitchcock, A. P.; Bazylinski, D. A.; Denes, P.; Joseph, J.; Lins, U.; Marchesini, S.; Shiu, H.-W.; Tyliszczak, T.; Shapiro, D. A. Measuring Spectroscopy and Magnetism of Extracted and Intracellular Magnetosomes Using Soft X-Ray Ptychography. *Proc. Natl. Acad. Sci. U.S.A.* **2016**, *113*, E8219−E8227.
(42) Wise, A. M.; Weker, J. N.; Kalirai, S.; Farmand, M.; Shapiro, D. A.; Meirer, F.; Weckhuysen, B. M. Nanoscale Chemical Imaging of an Individual Catalyst Particle with Soft X - Ray Ptychography. *ACS Catal.* **2016**, *6*, 2178−2181.
(43) Yu, Y.-S.; Kim, C.; Shapiro, D. A.; Farmand, M.; Qian, D.; Tyliszczak, T.; Kilcoyne, A. L. D.; Celestre, R.; Marchesini, S.; Joseph, J.; et al. Dependence on Crystal Size of the Nanoscale Chemical Phase Distribution and Fracture in $Li_xFePO_4$. *Nano Lett.* **2015**, *15*, 4282−4288.
(44) Bae, S.; Taylor, R.; Shapiro, D.; Denes, P.; Joseph, J.; Celestre, R.; Marchesini, S.; Padmore, H.; Tyliszczak, T.; Warwick, T.; et al. Soft X-Ray Ptychographic Imaging and Morphological Quantification of Calcium Silicate Hydrates (C − S − H). *J. Am. Ceram. Soc.* **2015**, *98*, 4090−4095.
(45) Shi, X.; Fischer, P.; Neu, V.; Elefant, D.; Lee, J. C. T.; Shapiro, D. A.; Farmand, M.; Tyliszczak, T.; Shiu, H.-W.; Marchesini, S.; et al. Soft X-Ray Ptychography Studies of Nanoscale Magnetic and Structural Correlations in Thin $SmCo_5$ Films. *Appl. Phys. Lett.* **2016**, *108*, 094103.
(46) Yu, Y.-S.; Farmand, M.; Kim, C.; Liu, Y.; Grey, C. P.; Strobridge, F. C.; Tyliszczak, T.; Celestre, R.; Denes, P.; Joseph, J.; Krishnan, H.; Maia, F. R. N. C.; Kilcoyne, A. L. D.; Marchesini, S.; Leite, T. P. C.; Warwick, T.; Padmore, H.; Cabana, J.; Shapiro, D. A. Three-dimensional Localization of Nanoscale Battery Reactions Using Soft X-Ray Tomography. *Nat. Commun.* **2018**, *9*, 921.
(47) Ade, H.; Hitchcock, A. P. NEXAFS Microscopy and Resonant Scattering: Composition and Orientation Probed in Real and Reciprocal Space. *Polymer* **2008**, *49*, 643−675.
(48) Shapiro, D. A.; Celestre, R.; Denes, P.; Farmand, M. Ptychographic Imaging of Nano-Materials at the Advanced Light Source with the Nanosurveyor Instrument. *J. Phys.: Conf. Ser.* **2016**, *849*, 012028.
(49) Marchesini, S.; Krishnan, H.; Daurer, B. J.; Shapiro, D. A.; Perciano, T.; Sethian, J. A.; Maia, F. R. N. C. SHARP: A Distributed GPU-Based Ptychographic Solver. *J. Appl. Crystallogr.* **2016**, *49*, 1245−1252.
(50) Hitchcock, A. P. aXis2000 Is Written in Interactive Data Language (IDL). It Is Available Free for Non-Commercial Use from http://unicorn.mcmaster.ca/aXis2000.html (accessed Feb 21, 2018).
(51) Yan, Z. B.; Hayes, R.; Melo, L. G. A.; Goward, G. R.; Hitchcock, A. P. X-Ray Absorption and Solid-State NMR Spectroscopy of Fluorinated Proton Conducting Polymers. *J. Phys. Chem. C* **2018**, *122*, 3233−3244.
(52) Saghi, Z.; Divitini, G.; Winter, B.; Leary, R.; Spiecker, E.; Ducati, C.; Midgley, P. A. Compressed Sensing Electron Tomography of Needle-Shaped Biological Specimens - Potential for Improved Reconstruction Fidelity with Reduced Dose. *Ultramicroscopy* **2016**, *160*, 230−238.
(53) Wu, J.; Lerotic, M.; Collins, S.; Leary, R.; Saghi, Z.; Midgley, P.; Berejnov, S.; Susac, D.; Stumper, J.; Singh, G.; et al. Optimization of Three-Dimensional (3D) Chemical Imaging by Soft X-Ray Spectro-Tomography Using a Compressed Sensing Algorithm. *Microsc. Microanal.* **2017**, *23*, 951−966.
(54) Lerotic, M.; Mak, R.; Wirick, S.; Meirer, F.; Jacobsen, C. MANTiS: A Program for the Analysis of X-Ray Spectromicroscopy Data. *J. Synchrotron Radiat.* **2014**, *21*, 1206−1212.
(55) Stalling, D.; Westerhoff, M.; Hege, H.-C. *Amira: A Highly Interactive System for Visual Data Analysis*; Zuse Institute Berlin, 2004.
(56) Banterle, N.; Bui, K. H.; Lemke, E. A.; Beck, M. Fourier Ring Correlation as a Resolution Criterion for Super-Resolution Microscopy. *J. Struct. Biol.* **2013**, *183*, 363−367.
(57) Saxton, W. O.; Baumeister, W. The Correlation Averaging of a Regularly Arranged Bacterial Cell Envelope Protein. *J. Microsc.* **1982**, *127*, 127−138.
(58) Jacobsen, C.; Wirick, S.; Flynn, G. J.; Zimba, C. Soft X-Ray Spectroscopy from Image Sequences with Sub-100 nm Spatial Resolution. *J. Microsc.* **2000**, *197*, 173−184.
(59) Koprinarov, I. N.; Hitchcock, A. P.; McCrory, C. T.; Childs, R. F. Quantitative Mapping of Structured Polymeric Systems Using Singular Value Decomposition Analysis of Soft X-Ray Images. *J. Phys. Chem. B* **2002**, *106*, 5358−5364.
(60) Otsu, N. A threshold Selection Method from Gray-Level Histograms. *IEEE Trans. Syst. Man Cybern. B Cybern.* **1979**, *9*, 62−66.
(61) Beckers, M.; Senkbeil, T.; Gorniak, T.; Reese, M.; Giewekemeyer, K.; Gleber, S.-C.; Salditt, T.; Rosenhahn, A. Chemical Contrast in Soft X-Ray Ptychography. *Phys. Rev. Lett.* **2011**, *107*, 208101.
(62) Leontowich, A. F. G.; Berg, R.; Regier, C. N.; Taylor, D. M.; Wang, J.; Beauregard, D.; Geilhufe, J.; Swirsky, J.; Wu, J.; Karunakaran,


DOI: 10.1021/acs.jpcc.8b02933
J. Phys. Chem. C 2018, 122, 11709−11719

C.: et al. Cryo Scanning Transmission X-Ray Microscope Optimized for Spectrotomography. *Rev. Sci Instruments*, submitted.
(63) Shapiro, D.; Roy, S.; Celestre, R.; Chao, W.; Doering, D.; Howells, M.; Kevan, S.; Kilcoyne, D.; Kirz, J.; Marchesini, S.; et al. Development of Coherent Scattering and Diffractive Imaging and the COSMIC Facility at the Advanced Light Source. *J. Phys.: Conf. Ser.* **2013**, *425*, 192011.



DOI: 10.1021/acs.jpcc.8b02933
*J. Phys. Chem. C* 2018, 122, 11709−11719